SUPPORTING INFORMATION

Thermoelectric Performance of Surface Engineered $Cu_{1.5-x}Te$-Cu_2Se nanocomposites

Congcong Xing,[a,b] Yu Zhang,[a,b]* Ke Xiao,[a,c] Xu Han,[d] Yu Liu,[e] Bingfei Nan,[a,c] Maria Garcia Ramon,[a,f] Khak Ho Lim,[g] Junshan Li,[h] Jordi Arbiol,[d, i] Bed Poudel,[b] Amin Nozariasbmarz,[b] Wenjie Li,[b] Maria Ibáñez,[f]* Andreu Cabot[a,i]*

[a] Catalonia Energy Research Institute - IREC, Sant Adrià de Besòs, 08930 Barcelona, Spain.

[b] Department of Materials Science and Engineering, Pennsylvania State University, University Park, Pennsylvania 16802, United States.

[c] University of Barcelona, Martí i Franqués 1, 08028, Barcelona, Spain.

[d] Catalan Institute of Nanoscience and Nanotechnology (ICN2), CSIC and BIST, Campus UAB, Bellaterra, 08193 Barcelona, Catalonia, Spain.

[e] School of Chemistry and Chemical Engineering, Hefei University of Technology, Hefei 230009, China.

[f] IST Austriansitute of Science and Technology Austria (ISTA), Am Campus 1, 3400 Klosterneuburg, Austria.

[g] Institute of Zhejiang University-Quzhou, 99 Zheda Rd, Quzhou 324000, Zhejiang, P.R. China.

[h] Institute for Advanced Study, Chengdu University, 610106, Chengdu, China.

[i] ICREA, Pg. Lluis Companys 23, 08010 Barcelona, Catalonia, Spain.

**E-mails:* Y. Zhang: *yvz5897@psu.edu;* M. Ibañez: *mibanez@ist.ac.at;* A. Cabot: *acabot@irec.cat*;

1. Synthesize and characterization on $Cu_{1.5}Te$ NPs.

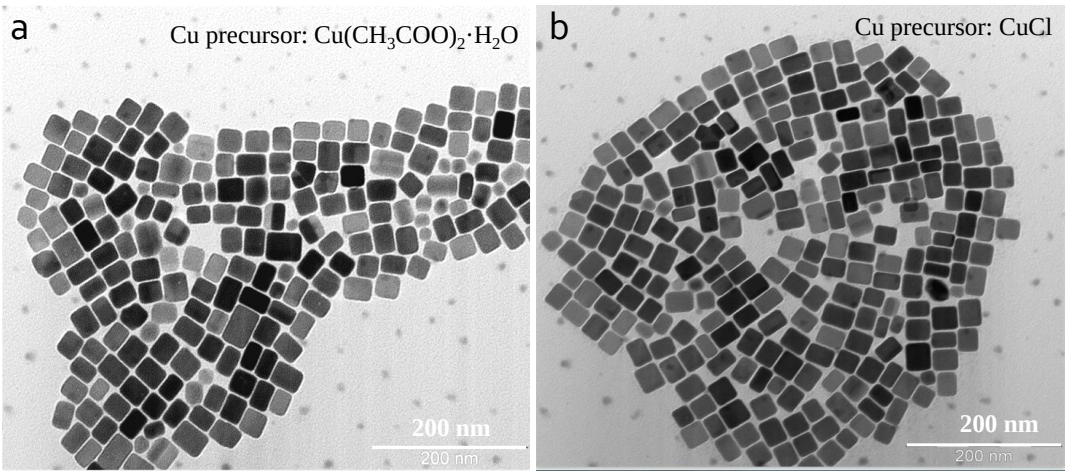

Figure S1. Representative TEM micrographs of the $Cu_{1.5}Te$ NPs synthesized from two different Cu precursors: (a) $Cu(CH_3COO)_2 \cdot H_2O$ and (b) CuCl.

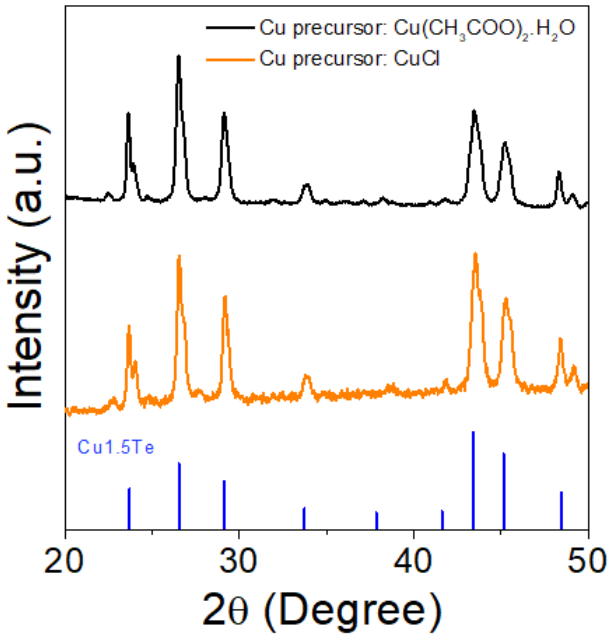

Figure S2. comparison of powder XRD patterns of as-synthesized $Cu_{1.5}Te$ NPs produced from two precursors: $Cu(CH_3COO)_2 \cdot H_2O$ (black color) and CuCl (orange color). The reference pattern for the simulated XRD pattern of $Cu_{1.5}Te$ are also displayed.

a

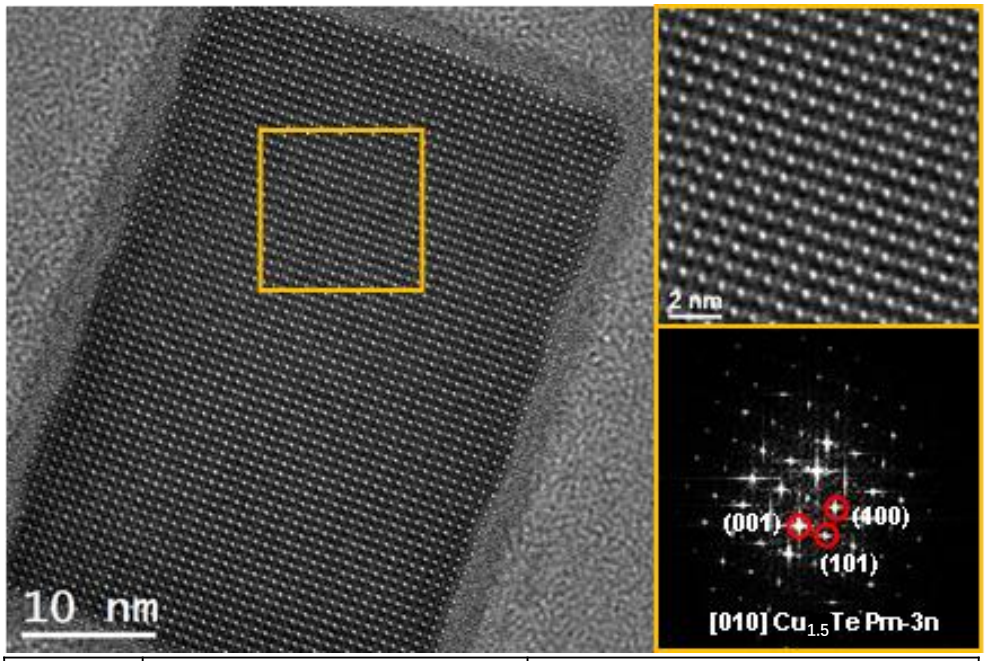

b

Spot	Experimental (nm)	$Cu_{1.5}Te$ (Pm-3n) [010]
1	0.734	0.751 (001)
2	0.532 (43.44º vs Spot 1)	0.531(45.00º) (101)
3	0.728 (88.78º vs Spot 1)	0.751 (90.00º) (100)

Figure S3. (a) Additional HRTEM micrograph taken from the $Cu_{1.5}Te$ sample. Detail of the orange squared region and its corresponding power spectrum which reveals that this nanostructure has a crystal phase that is assigned to the $Cu_{1.5}Te$ cubic phase (space group = Pm-3n) with a=b=c=7.5100 Å. From the crystalline domain, the $Cu_{1.5}Te$ lattice fringe distances were measured to be 0.734 nm, 0.532 nm and 0.728 nm, at 43.44º and 88.78º which corresponds to the $Cu_{1.5}Te$ cubic phase, visualized along its [010] zone axis. (b) Comparison between the experimental and the theoretical bulk plane spacing distances and angles between planes.

2. Surface treatment with SeL solution.

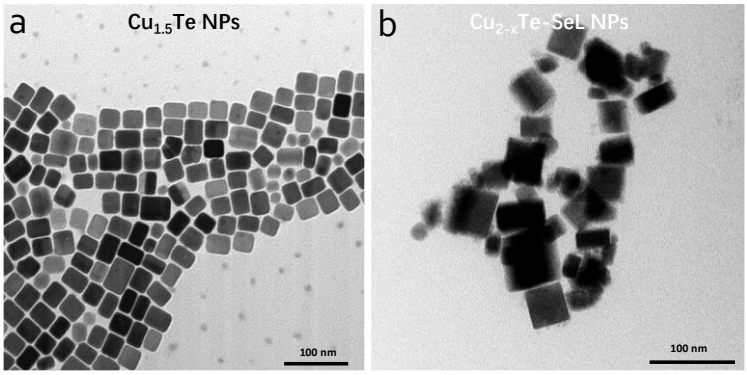

Figure S4. Representative TEM micrographs of $Cu_{1.5}Te$ nanoparticles (NPs) (a) before and (b) after SeL treatment. It is evident from the images that the NPs aggregate after surface treatment with SeL.

a

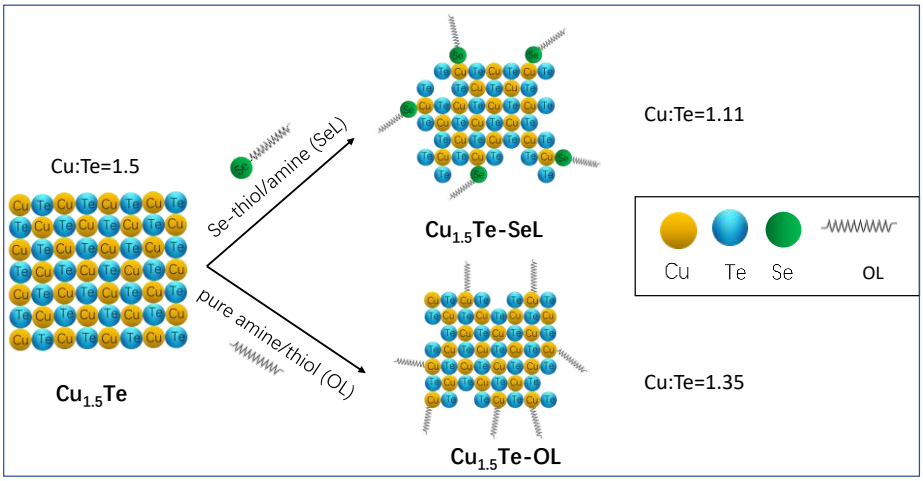

b

Element \ Sample (at%)	$Cu_{1.5}Te$	$Cu_{1.5}Te$-OL	$Cu_{1.5}Te$-SeL	$Cu_{1.5}Te$-SeL supernatant
Cu	61.5	56.4	51.1	39.7
Te	38.5	41.7	45.7	4.2
Se	0	0	2.5	7.0
S	0	1.9	0.7	49.1

Figure S5. (a) Schematic illustration of two surface treatment procedures on $Cu_{1.5}Te$ NPs. (b) Composition of $Cu_{1.5}Te$ NPs, $Cu_{1.5}Te$-OL NPs, $Cu_{1.5}Te$-SeL NPs and $Cu_{1.5}Te$-SeL supernatant obtained from ICP analysis.

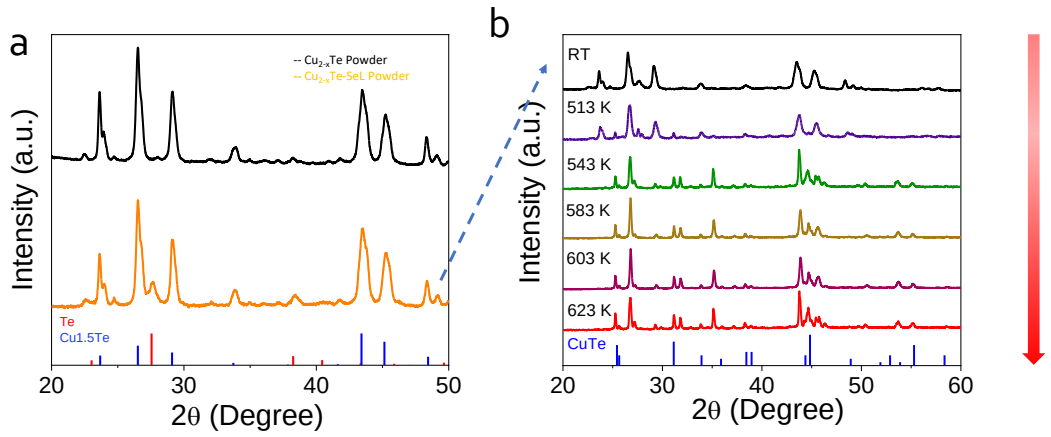

Figure S6. (a) Powder XRD pattern of $Cu_{1.5}Te$ (black) and $Cu_{1.5}Te$-SeL (orange) powder before annealing. The standard diffraction pattern of Te and $Cu_{1.5}Te$ are included as reference. (b) XRD pattern of $Cu_{1.5}Te$-SeL powder after annealing at different temperature, indicating phase evolution during thermal treatment. The standard diffraction pattern of CuTe (JCPDS No. 00-022-0252) is included as reference.

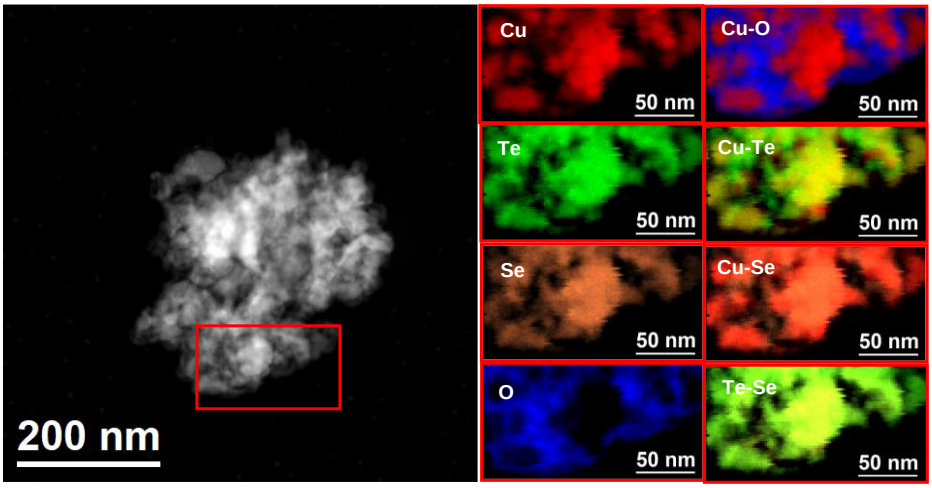

Figure S7. Additional EELS chemical composition maps of annealed $Cu_{1.5}Te$-SeL particles obtained from the red squared area in the STEM micrograph. Individual Cu $L_{2,3}$-edge at 931 eV (red), Te $M_{4,5}$-edge at 572 eV (green) Se $L_{2,3}$ –edge 1436 eV(orange) and O K-edge at 532 eV (blue) as well as its composites.

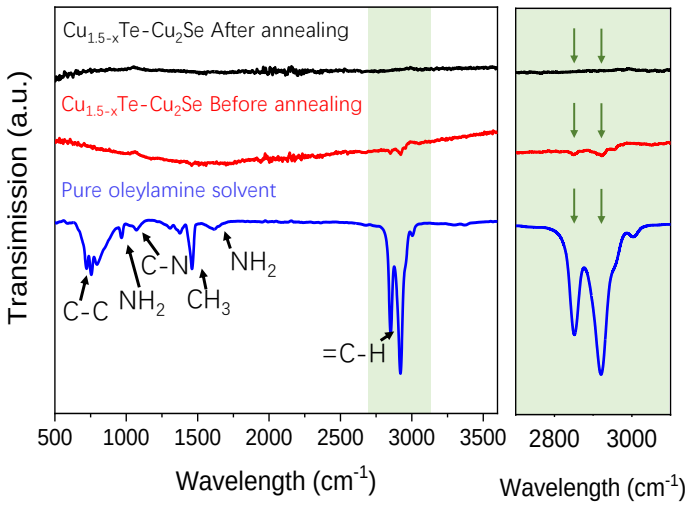

Figure S8. FTIR Spectra of $Cu_{1.5-x}Te$-Cu_2Se nanocomposites before and after annealing at 623 K for 1 h under Ar flow.

a

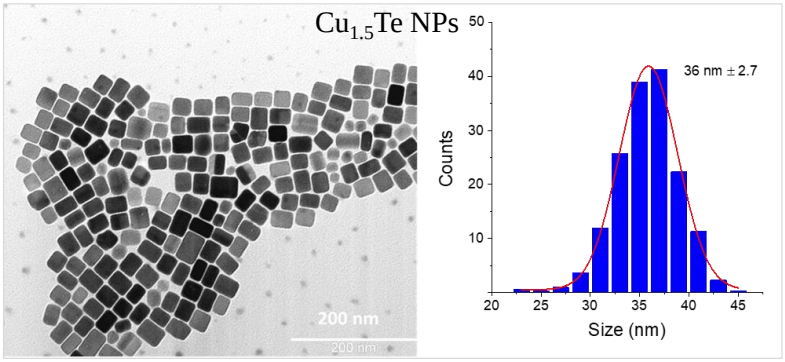

b

	Nanoparticles	Size (nm)
	$Cu_{1.5}Te$-SeL	41
Annealled $Cu_{1.5}Te$	CuTe	46
	$Cu_{2.72}Te_2$	45
annealed $Cu_{1.5-x}Te$-Cu_2Se nanocomposites	$Cu_{1.81}Te$	49
	$Cu_{2.72}Te_2$	81

Figure S9. (a) TEM images and size distribution histograms of $Cu_{1.5}Te$ NPs. (b) Average crystallite size of $Cu_{1.5}Te$-SeL NPs, CuTe NPs, $Cu_{2.72}Te_2$ NPs and $Cu_{1.81}Te$ NPs calculated using Scherrer equation.

3. Characterization on consolidated pellets.

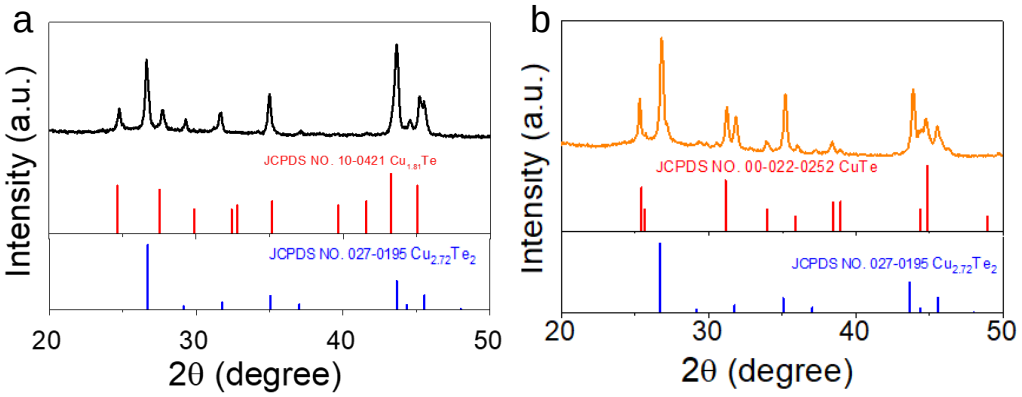

Figure S10. XRD patterns of consolidated (a) $Cu_{1.5}Te$ and (b) $Cu_{1.5}Te$-SeL pellets, the standard diffraction patterns of $Cu_{1.81}Te$ (JCPDS No. 10-0421), CuTe (JCPDS No. 00-022-0252) and $Cu_{2.72}Te_2$ (JCPDS No. 00-043-1401) are included as reference.

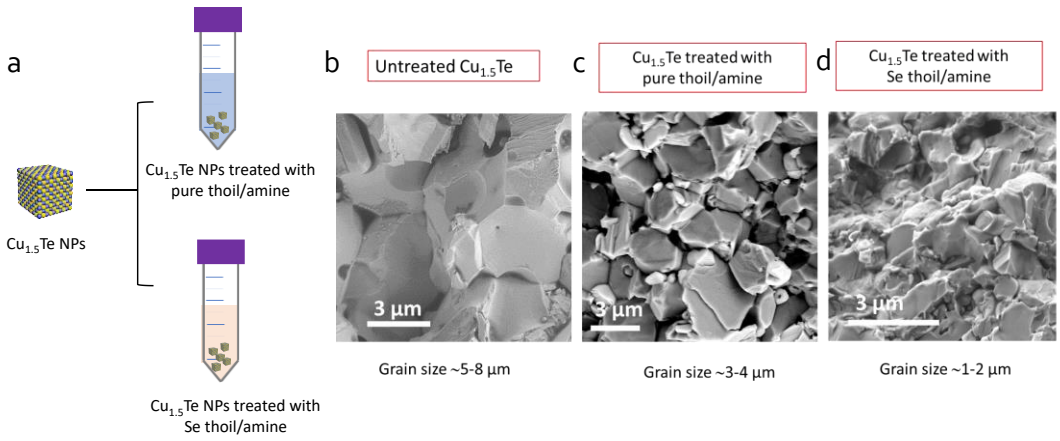

Figure S11. (a) Schematic illustration of post synthetic treatment of $Cu_{1.5}Te$ NPs with different ligands. Corresponding cross-sectional SEM images of (b) $Cu_{1.5}Te$ pellet, (c) $Cu_{1.5}Te$-OL, and (d) $Cu_{1.5-x}Te$-Cu_2Se pellets.

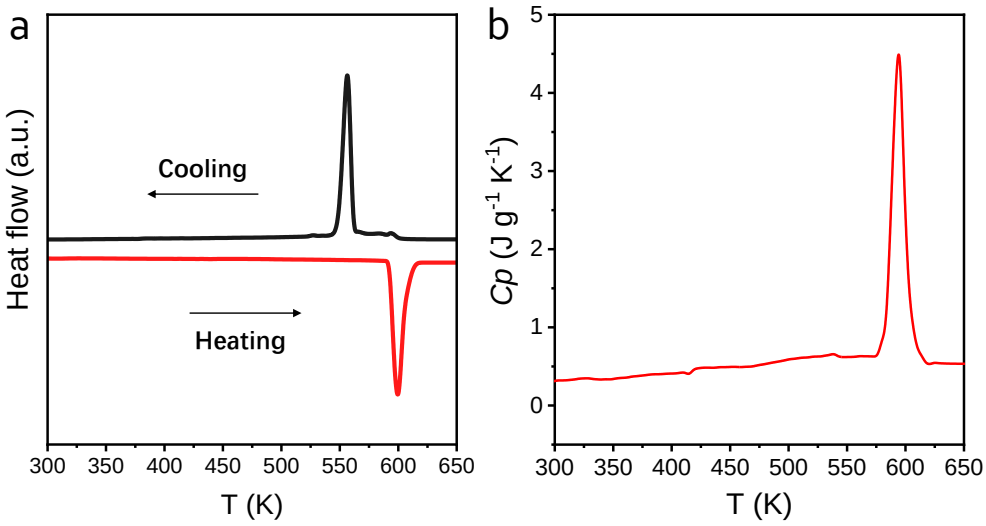

Figure S12. (a) Differential scanning calorimetry (DSC) curves of $Cu_{1.5-x}Te$-Cu_2Se pellet collected in a consecutive heating (red) and cooling (black) cycle. (b) Specific heat of $Cu_{1.5-x}Te$-Cu_2Se pellet.

4. High temperature XRD and TE properties.

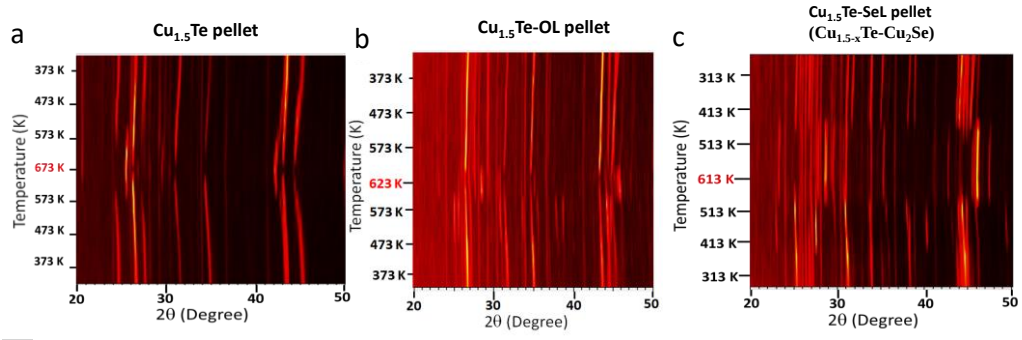

Figure S13. (a) 2D heatmap of in-situ XRD characterization on: (a) $Cu_{1.5}Te$ (untreated) pellet; (b) $Cu_{1.5}Te$-OL (treated with thiol/amine ligands only) pellet; and (c) $Cu_{1.5}Te$-SeL (treated with Se ligands) pellet in a complete heating-cooling (bottom-top) cycle.

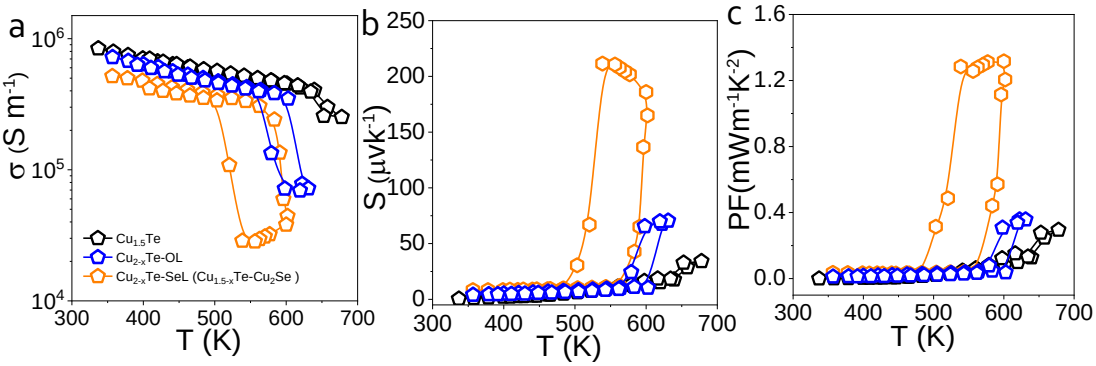

Figure S14. Temperature dependence of thermoelectric properties of $Cu_{1.5}Te$ (⬠), $Cu_{1.5}Te$-OL (⬠) and $Cu_{1.5-x}Te$-Cu_2Se (⬠) pellets in a consecutive heating and cooling process: (a) electric conductivity, σ; (b) Seebeck coefficient, S; and (c) power factor, PF.

5. Stability and repeatability.

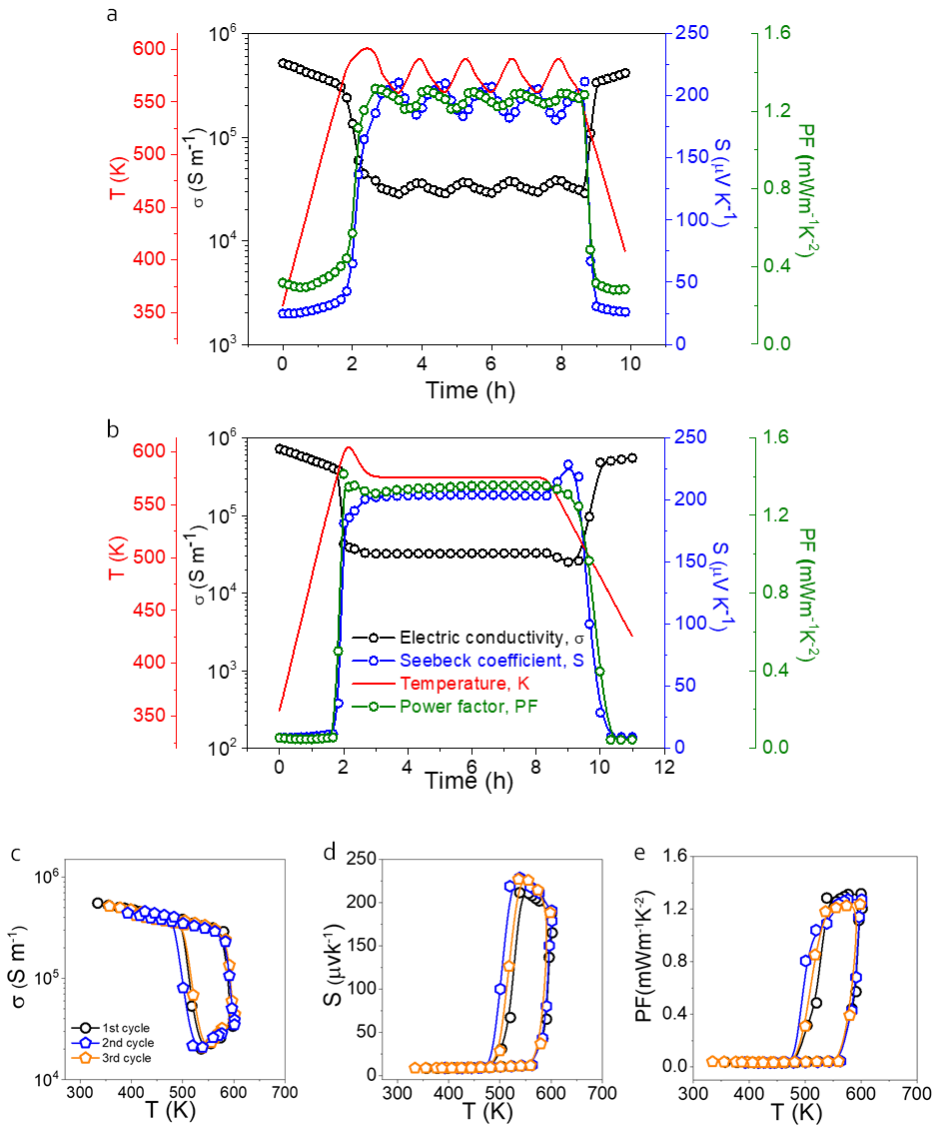

Figure S15. (a) Evolution of the electrical conductivity (σ), Seebeck coefficient (S) and power factor (PF) of the $Cu_{1.5-x}Te$-Cu_2Se sample for 5 consecutive heating-cooling cycles at a temperature range between 540 K and 590 K. (b) Time evolution of the $Cu_{1.5}Te$-SeL sample during 10 h test. Reversibility of TE properties of $Cu_{1.5-x}Te$-Cu_2Se sample with several heating-cooling cycles: temperature-dependent TE performance of (c) electrical conductivity, (d) Seebeck coefficient and (e) power factor.

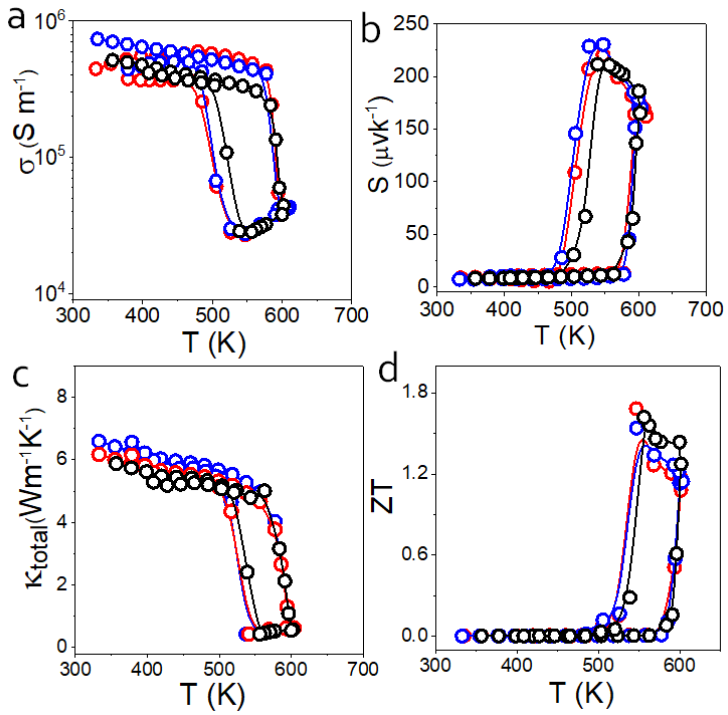

Figure S16. Temperature dependence of electrical conductivity, σ (a); Seebeck coefficient, S (b); thermal conductivity, κ (c); and TE figure of merit, ZT (d) of three $Cu_{1.5}Te$-SeL pellets measured in heating and cooling cycle. Data from 3 samples is plotted with black, red, and blue circles, respectively.

6. Anisotropic characterizations.

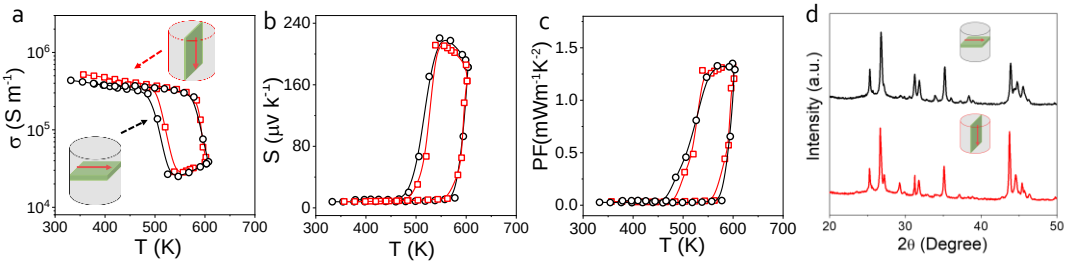

Figure S17. Anisotropic characterizations. Temperature dependence of electrical conductivity, σ (a); Seebeck coefficient, S (b); power factor, PF (c) and XRD patterns (d) of $Cu_{1.5-x}Te$-Cu_2Se pellet in parallel and perpendicular directions.

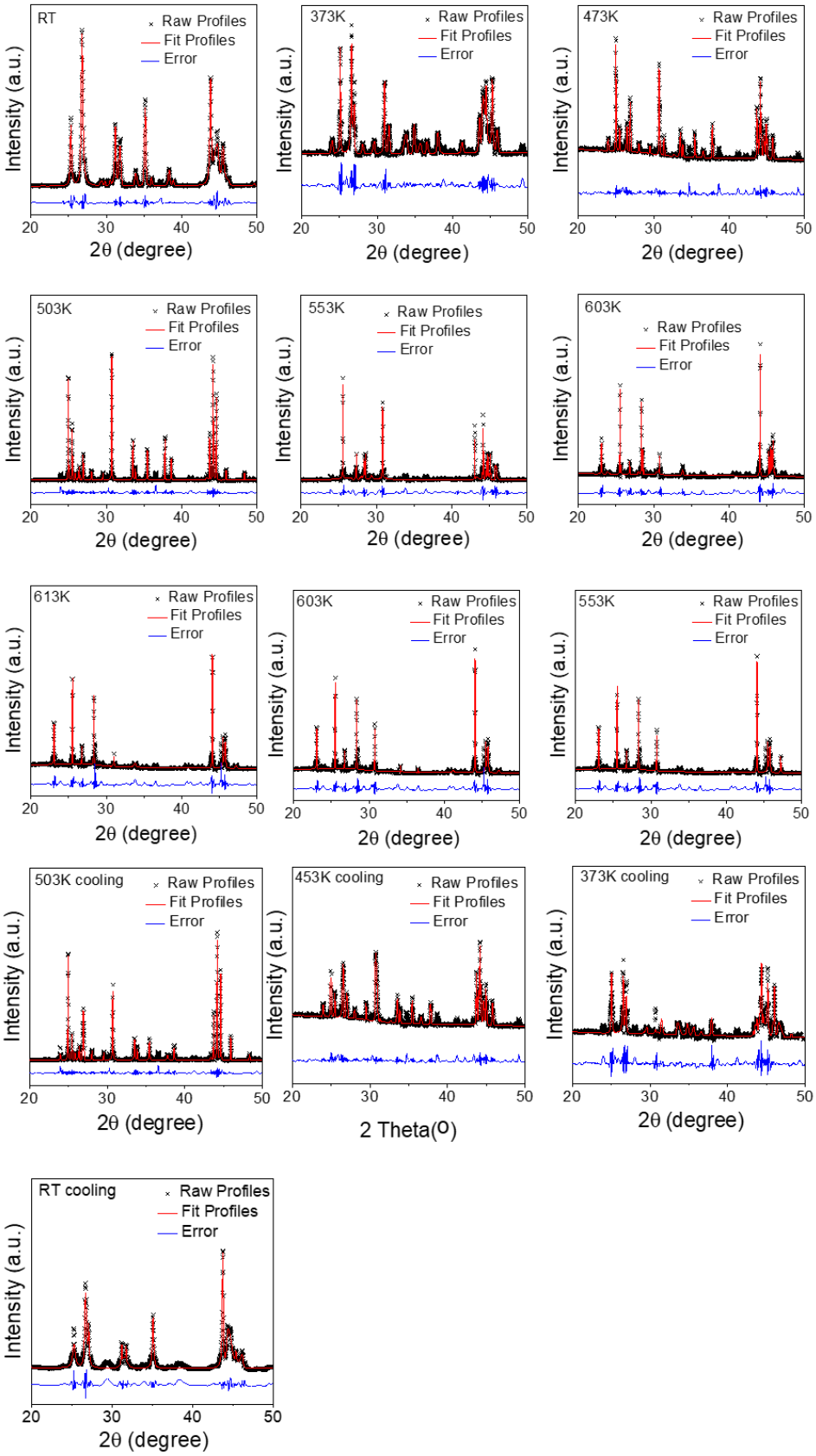

Figure S18. The Rietveld refinement of in-situ XRD patterns of $Cu_{1.5-x}Te$-Cu_2Se pellet at different temperatures.

Table S1. Refined lattice parameters (from Rietveld refinement of the XRD patterns) of different crystal structures at corresponding temperatures.

Temp	Phase	a (Å)	b (Å)	c (Å)	Area%
RT	$Cu_{2.86}Te_2$	3.976	3.932	6.119	35.1
	CuTe	3.143	4.080	7.010	64.9
373K	$Cu_{2.86}Te_2$	4.002	3.945	6.110	37.0
	CuTe	3.150	4.077	7.157	63.0
473K	$Cu_{2.86}Te_2$	4.037	3.956	6.087	35.8
	CuTe	3.134	4.142	6.939	65.2
503K	$Cu_{2.86}Te_2$	4.056	3.937	6.084	36.7
	CuTe	3.163	4.096	6.925	63.3
553K	$Cu_{2.86}Te_2$	3.995	3.976	6.144	33.6
	CuTe	3.160	4.078	6.932	66.4
603K	$Cu_{2.86}Te_2$	3.991	3.965	6.110	31.5
	Cu_4Te_3	8.306	8.306	2.110	33.4
	Te	4.458	4.458	5.927	35.1
613K	$Cu_{2.86}Te_2$	3.983	3.957	6.156	31.8
	Cu_4Te_3	8.313	8.311	2.115	32.7
	Te	4.447	4.447	5.9346	35.4
603K	$Cu_{2.86}Te_2$	3.991	3.965	6.110	34.5
	Cu_4Te_3	8.310	8.308	2.114	31.8
	Te	4.458	4.458	5.927	33.7
553K	$Cu_{2.86}Te_2$	3.995	3.976	6.144	31.1
	Cu_4Te_3	8.301	8.303	2.107	35.2
	Te	4.433	4.419	6.222	33.7
503K	$Cu_{2.86}Te_2$	3.934	3.917	6.221	33.0
	CuTe	3.231	4.102	6.751	67.0
453K	$Cu_{2.86}Te_2$	3.994	3.978	6.123	34.5
	CuTe	3.161	4.079	6.928	65.5
373K	$Cu_{2.86}Te_2$	4.011	3.943	6.117	31.6
	CuTe	3.155	4.079	7.029	68.4
RT	$Cu_{2.86}Te_2$	3.987	3.963	6.109	65.0
	CuTe	3.140	4.078	6.980	35.0

Table S2. Relative densities of $Cu_{1.5}Te$, $Cu_{1.5-x}Te$-OL and $Cu_{1.5-x}Te$-Cu_2Se pellets obtained from absolute values measured with the Archimedes' method.

Sample	$Cu_{1.5}Te$	$Cu_{1.5-x}Te$-OL	$Cu_{1.5-x}Te$-Cu_2Se
Crystal density (g/cm^3)	6.16	6.42	6.59
Measured density (g/cm^3)	5.79	6.12	6.07
Relative density	93.9%	95.3%	92.1%